



Hydrogen-induced enhancement of thermal stability in VZr(H) metallic glasses

Maciej Kaplan^a, Johan Bylin^a, Paulius Malinovskis^a, Ralph H. Scheicher^b, Gunnar K. Pálsson^{a,*}

^a Division of Materials Physics, Department of Physics and Astronomy, Uppsala University, Box 516, Uppsala, SE-75121, Sweden

^b Division of Materials Theory, Department of Physics and Astronomy, Uppsala University, Box 516, Uppsala, SE-75121, Sweden



ARTICLE INFO

Keywords:

Metallic glass
Hydrogen in metals
Thermal stability
Thermodynamic driving force
Density functional theory
In-situ experiments

ABSTRACT

Prediction of crystallization temperatures in metallic glasses is still an open question. Investigations of multi component alloys are common in the literature, however, binary and ternary alloys are more suitable for fundamental studies due to their simplicity. Here, we show that a low thermodynamic driving force for crystallization can be associated with a high crystallization temperature. The driving force is determined by calculating – for the first time in metallic glasses – the temperature dependent Gibbs free energies of the alloys using *ab initio* density functional theory, in combination with the stochastic quenching method. The crystallization temperatures of V_xZr_{100-x} and $V_xZr_{67-x}H_{33}$ have been determined using simultaneous *in-situ* x-ray scattering techniques and resistivity measurements. The onset of crystallization is found to exhibit a parabolic dependence throughout the composition range, whereas alloying with hydrogen increases the thermal stability up to 150 K close to the amorphous-crystalline boundaries. These findings suggest that hydrogen acts as an alloying element with the ability to dynamically tune the intrinsic properties of the material. Lastly, temperature-dependent descriptions of the Gibbs free energy and kinetic considerations of a metallic glass are necessary for a complete characterization of the crystallization process.

1. Introduction

Metallic glasses lack atomic long-range order and can be considered as being free from grains, grain boundaries, and other topological defects otherwise present in crystalline materials. The absence of local defects in metallic glasses, such as dislocations, give rise to a higher elastic deformation limit, up to 6.6 % (Ref. [1,2]), while crystalline materials rarely exceed 1 % (Ref. [3]). Metallic glasses can therefore be less prone to mechanical failure during hydrogenation and can store more hydrogen compared to crystalline counterparts [4]. Furthermore, metallic glasses are less susceptible to hydrogen embrittlement. Variation of the hydrogen-induced expansion in different hydride phases, and accumulation of hydrogen at the grain boundaries in crystalline materials can result in mechanical failure [5]. Hydrogen-embrittlement in metallic glasses can occur, but is largely attributed to the formation of nano and micro crystallites during heating [6]. It is therefore important to examine the thermal stability of metallic glasses, to determine at what temperature crystallization occurs [7], for the possibility to create robust hydrogen storage materials that are unaffected to hydrogen-induced embrittlement [6,8,9]. It has been shown that the presence of hydrogen in some materials can alter the stability of metallic glasses,

either by lowering the crystallization temperature by 300 K [10] or increase it up to 40 K [11–13].

The amorphous state can be viewed as a single-phase solid solution [14] and the distribution of the elements can be seen as homogeneous on length scales larger than a few nanometers [15]. High amounts of an element can be dissolved in the amorphous state, while in crystalline alloys the solubility is bound by the principles of thermodynamics, imposing composition restrictions on each constituting phase. Therefore, a wider composition range compared to a crystal is accessible in the amorphous state, making it possible to fine-tune the elemental ratios and thus influence the properties of the alloy. The chemical composition is crucial for the formation and thermal stability of metallic glasses, but the most important parameters are found empirically to be the elemental melting points [16], atomic size mismatch [17,18], and the liquid mixing enthalpies among the constituents [19].

To understand the influence of hydrogen on the thermal stability of metallic glasses one has to select an alloy system where glass formation is possible and where the elements have an affinity to absorb hydrogen. Binary systems, due to their simplicity, are preferred over multicomponent alloys for a fundamental study, but have in general lower glass forming ability [19]. V and Zr are suitable elements due to their atomic

* Corresponding author.

E-mail address: gunnar.palsson@physics.uu.se (G.K. Pálsson).

size mismatch, mixing enthalpy, melting points, and affinity for hydrogen absorption. Hydrogen in crystalline VZr is a well-studied material, and is well known for its exceedingly large volumetric density [9]. It has also been used as cathode material in metal hydride batteries and it is a potential replacement material for palladium as a purifying membrane in its metallic glass [20]. Amorphous VZr alloys, have been studied with respect to their thermal stability [21,22], however, the hydrogen uptake, resistance to hydrogen-induced embrittlement, and thermal stability of the amorphous $V_xZr_{67-x}H_{33}$ alloys is not known.

In this work, we evaluate the effect of hydrogen on the thermal stability of metallic glasses using amorphous VZr(H) thin films as a model system. To do so, the electrical resistivity, x-ray reflectometry (XRR), and x-ray diffraction (XRD) were measured *in-situ* during several annealing cycles in vacuum and hydrogen atmosphere using an ultra high vacuum (UHV) compatible chamber. The methodology was carried out to determine the influence of hydrogen and the heat treatment on the structure of the films. First-principles calculations were used to determine the thermodynamic driving force for crystallisation of the amorphous VZr(H) alloys. The electronic, phononic and configurational contributions to the temperature dependent Gibbs energies of the amorphous alloys and their corresponding crystalline states were calculated.

2. Experimental and theoretical details

V_xZr_{100-x} films of nominally 100 nm were deposited on sapphire (Al_2O_3) substrates using direct current magnetron sputtering and capped with 5 nm Al_2O_3 to prevent oxidation. It has been shown that hydrogen is able to permeate through thin Al_2O_3 layers at elevated temperature and hydrogen pressures [23]. This asymmetric energy barrier prevents desorption during quick heating cycles. The base pressure of the sputter chamber was 3.6×10^{-10} Torr and all depositions were made at an Ar pressure of 2.5 mTorr. The deposition rate of each target material was calibrated by determining thickness and density of reference films using x-ray reflectometry. The composition of each film was verified with Rutherford backscattering spectrometry. Temperature dependent x-ray and resistivity measurements were performed in a custom-built *in-situ* UHV compatible chamber with a base pressure of $3.9 \cdot 10^{-9}$ Torr, mounted on a Bruker D8 Discover diffractometer. The alloys have been annealed with a sawtooth profile (see inset Fig. 3) with a rate of 3 K/min, from 403 to 923 K, until crystallization was detected. The diffractometer is equipped with a line focused $CuK\alpha$ radiation source and a Göbel mirror. The structure of the films was determined using grazing incidence x-ray diffraction at an incidence of 1.2 deg, a primary slit of 0.1 mm and 2 mm anti-scatter and detector slits. The thickness of each film was determined using XRR with a 0.05 mm primary slit, 0.6 mm anti-scatter slit, and 0.1 mm detector slit. The reflectivity patterns were fitted using the GenX software [24], which includes multiple scattering, x-ray absorption, resolution and background effects.

The temperature was monitored with a type K thermocouple attached on the sample surface. Hydrogen gas was introduced from a metal hydride in the chamber, and a capacitance pressure gauge was used to read the H_2 pressure. The pressure for annealing in hydrogen was set to 95 Torr to ensure that a hydrogen concentration of at least 33 at.% was reached. Subsequent nuclear reaction analysis verified that this pressure corresponds approximately 33 at.% H. Due to the protective oxide cap layer and the relatively fast heating and cooling rates, the hydrogen concentration is judged to be fairly constant throughout the annealing. UHV conditions are important when studying the thermal properties of a material: the thermal energy will eventually be comparable to the activation energy of chemical reactions, making it more likely for the ambient environment to react with the sample. For instance, the onset of oxidation can occur at elevated temperatures even when capping layers are used [18]. Protection against oxidation is especially important for Zr-containing alloys due its large affinity for oxygen.

The *in-situ* chamber has motorized four-point measuring probes for resistivity measurements which enables high precision between mea-

surements. A Keithley 2400 Source Meter was used in delta mode (thereby removing both contact resistance and thermally induced emfs) and a Keithley 2182A Nanovoltmeter was used to measure the voltage. The measured voltage is directly corresponding to the voltage within the VZr(H) alloy, since the substrate and capping materials are both insulating materials (Al_2O_3). The voltage is used to calculate the absolute resistivity of the VZr(H) alloy [25]:

$$\rho = C \frac{\pi}{\ln(2)} \frac{U}{I} \frac{1}{t}, \quad (1)$$

where C is the geometry factor, U the measured voltage (V), I the current (A), and t the film thickness (Å). The geometry factor for the resistivity was determined by reference measurements of a Nb foil in the *in-situ* chamber and between 4–300 K in a different setup. The temperature coefficient of the resistivity (α) and crystallization temperature (T_x) are determined using the resistivity data. Crystallization is detected by two signatures in the resistivity of the VZr(H) alloys: a sudden decrease in resistivity at the crystallization event, and change from negative to positive value of α . The crystallization event is subsequently verified with *in-situ* XRD, and complementary XRR provide additional insight on the integrity of the films.

For the first-principles calculations, amorphous configurations were generated via the stochastic quenching method [26] using density functional theory [27,28] (DFT), as implemented by the Vienna Ab initio simulation package (VASP) [29–31], using the generalized gradient approximation correlation-functional of Perdew, Burke and Ernzerhof [32]. The stochastic quenching procedure is used to generate amorphous supercells starting from a random configuration of atomic positions, separated by at least one atomic radii, that are subsequently allowed to relax until the Feynman-Hellman forces are below a predefined threshold. For our purposes, a supercell of size $14 \text{ Å} \times 14 \text{ Å} \times 14 \text{ Å}$, computed with an energy cut-off of 450 eV and projector augmented wavefunction pseudopotentials with semi-core states in the valence state was found to represent the configurational space of the amorphous systems and its collection of electronic levels. Given the size of the supercell, only the Γ k-point was needed to relax the structures, in which the force and energy convergence threshold criteria were set to 20 meV/Å and 10^{-6} eV respectively. Once the candidate structures had been determined, the total energy and the electronic density of states were calculated using a more accurate $3 \times 3 \times 3$ k-points Monkhorst-Pack mesh, with Methfessel-Paxton smearing [33] 0.4 eV. The Phonopy package [34] was used to calculate the phononic density of states, in which only the Γ k-point was used for the amorphous supercells due to the sheer number of explicit atomic displacement calculations.

To introduce hydrogen into the metallic systems, we implemented a procedure which inserted hydrogen atoms at random into the initial candidate metal structures under the constraint that no hydrogen atom could be placed closer than 1.9 Å to any other atom. Thereafter, the volume of the cells were varied in a series of steps, allowing the coordinates of the atoms to fully relax before the cells exhibiting an external pressure magnitude below 3 kbar could be extracted and used for the energy and density of states calculations.

To make the calculations tractable we have excluded the effect of thermal expansion. The structure of all simulated materials exhibit zero external pressure. The Gibbs free energy is approximated as follows:

$$G(T) \approx U_0 + U_{el}(T) + U_{ph}(T) - T[S_{el}(T) + S_{ph}(T) + S_{mix}] \quad (2)$$

where U_0 is the ground state energy, $U_{el}(T)$ and $S_{el}(T)$ are the free energy and entropy associated with electronic excitations, $U_{ph}(T)$ and $S_{ph}(T)$ are the free phonon energy and entropy and S_{mix} is the entropy related to mixing the atomic species, given by

$$S_{mix} = -k_B \sum_i x_i \ln x_i \quad (3)$$

where x_i is the atomic fraction of species i in the material. The electronic and phononic free energies are computed via the integration of

the electronic and phononic density of states respectively, via

$$U_{el}(T) = \int_0^\infty E n(E, T) D_{el}(E) dE - \int_0^{E_F} E D_{el}(E) dE \quad (4)$$

and

$$U_{ph}(T) = 3 \int_0^\infty \hbar \omega \left[\frac{1}{2} + \tilde{n}(\hbar \omega, T) \right] D_{ph}(\omega) d\omega \quad (5)$$

where n and \tilde{n} are each corresponding to the Fermi-Dirac and Bose-Einstein distribution, and D_{el} and D_{ph} are the density of electron and phonon states respectively. To compute the entropy, we use

$$S_{el}(T) = -k_B \int_0^\infty D_{el} [n \ln n + (1 - n) \ln(1 - n)] dE \quad (6)$$

and

$$S_{ph}(T) = 3k_B \int_0^\infty D_{ph} [(\tilde{n} + 1) \ln(\tilde{n} + 1) - \tilde{n} \ln \tilde{n}] d\omega. \quad (7)$$

To compute the thermodynamic driving force for the V_xZr_{100-x} alloys we chose the reference Gibbs free energy as a mixture of the unreacted crystalline bcc Zr and hcp Zr, whereas for the $V_xZr_{67-x}H_{33}$ alloys the bcc V_2H and bcc Zr_2H solid solutions were used. It is important to note that the entropy of mixing for pure elements is zero, and is likewise zero for the mixing between V or Zr and H in the V_2H and Zr_2H structures because they fill two separate sublattices [35,36]. A configurational contribution to the entropy of mixing nonetheless exists for the hydrogen, which corresponds to the mixing of H and vacancies among the available sites in the bcc lattices. We assume herein that the number of vacant sites for hydrogen to fill are one per metal atom, which implies that for V_2H and Zr_2H , we fill half of the available sites. Hence, the entropy of mixing for H in the bcc structures is $k_B \ln 2$ according to Eq. (3). However, the entropy of mixing is determined for the amorphous $V_xZr_{67-x}H_{33}$ alloys via Eq. (3). This is because every configuration of VZr generates a unique configuration of available sites for H, which on average is equivalent to a homogeneous mixing of the elements. A better representation of the configurational entropy which could capture the entropy related to the correlations of hydrogen sites to metal atoms is however discussed in the following section. The difference in the Gibbs free energy is calculated by:

$$\Delta G = G_c - G_a, \quad (8)$$

where G_a is the Gibbs free energy of the amorphous state, G_c is the Gibbs free energy of the corresponding crystalline reference state. The thermodynamic driving force used herein is defined as $-\Delta G$.

3. Results and discussion

The investigated alloys are V_xZr_{100-x} , where $x = 80, 67, 50, 33$ at.% (unless otherwise stated), and the alloys containing hydrogen were $V_xZr_{67-x}H_{33}$, where $x = 54, 45, 34$, and 17 at.%. The ratio of V and Zr is kept constant for the alloys with and without hydrogen, e.g. $V_{80}Zr_{20}$ and $V_{54}Zr_{13}H_{33}$ have the same V/Zr ratio. Measured and fitted reflectivity patterns are shown in Fig. 1, from which the thickness, roughness, and densities of the individual layers in each sample are determined by using the GenX software [24]. All samples have low roughness, are uniform, and each V_xZr_{100-x} layer thickness is close to 1000 Å. Both film uniformity and thickness are important for an accurate absolute resistivity determination, which is calculated according to Eq. (1).

The diffractograms of the as-grown alloys are shown in Fig. 2, where a broad peak (halo) between 35–40 degrees (2.5 – 2.8 Å⁻¹) can be identified. The position and intensity of the halo varies systematically with respect to composition. The variation stems from a Fourier transform of a weighted sum of the average nearest neighbor distance of the three partial pair distribution functions of the V-V, Zr-Zr and the V-Zr pairs, as

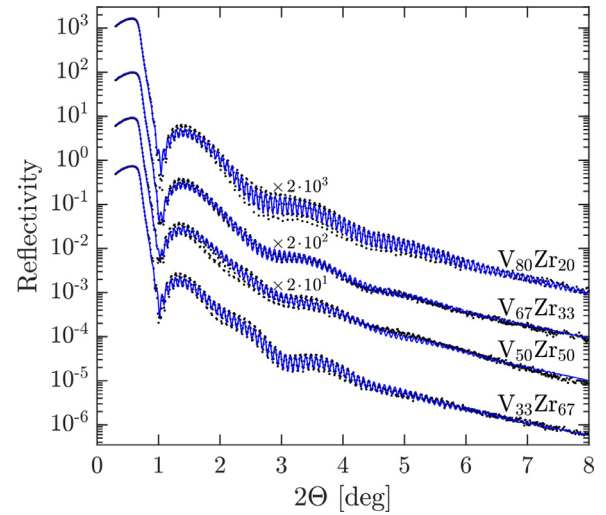


Fig. 1. X-ray reflectivity of the as-deposited V_xZr_{100-x} alloys together with a slab model fit using the GenX software. The fit confirms the intended thickness, and reveals good layering of the films and compact structure.

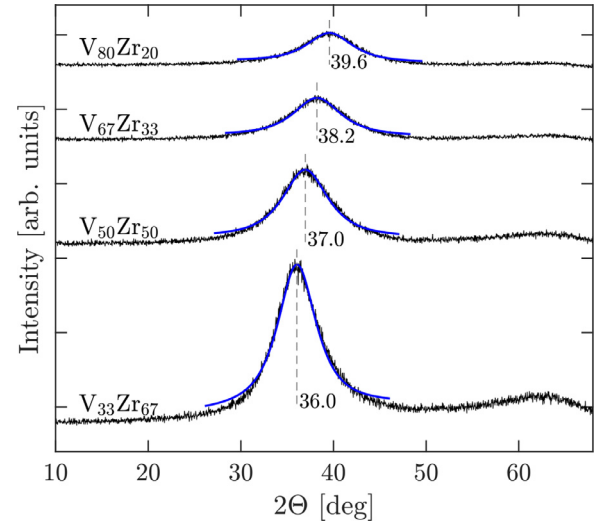


Fig. 2. Grazing incidence x-ray diffraction of the as-deposited V_xZr_{100-x} alloys. A broad diffuse peak is clearly seen in the diffractogram, typical of an amorphous structure. The peaks were fitted using a mixture of Gaussian and Lorentzian functions (pseudo-Voigt) and are shown as blue lines and the position of peaks are shown by the dashed gray lines. (For interpretation of the references to colour in this figure legend, the reader is referred to the web version of this article.)

well as their respective cross-section. The angular range available using grazing incidence diffraction is limited by the *in-situ* resistivity setup, however, no evidence of diffraction peaks at higher angles was found using another diffractometer between 10 degrees and 155 degrees.

The temperature dependence of the resistivity, ρ , for the $V_{67}Zr_{33}$ alloy is shown in Fig. 3a, and the temperature profile which was applied for this alloy is shown in the top-right inset. The observed resistivity decreases when the material is heated and the opposite is noted during cooling. Hence, the material has a negative temperature coefficient of resistivity, α , which is common for amorphous alloys. For metals and alloys, the α generally decreases with increasing ρ and has a crossover from positive to negative around 100–200 $\mu\Omega\text{cm}$ [37]. At temperatures exceeding 500 K, ρ is seen to increase irreversibly, while α remains negative upon cooling. The $V_{67}Zr_{33}$ alloy remains amorphous, which is verified by XRD measurements. The irreversible increase can be due to re-

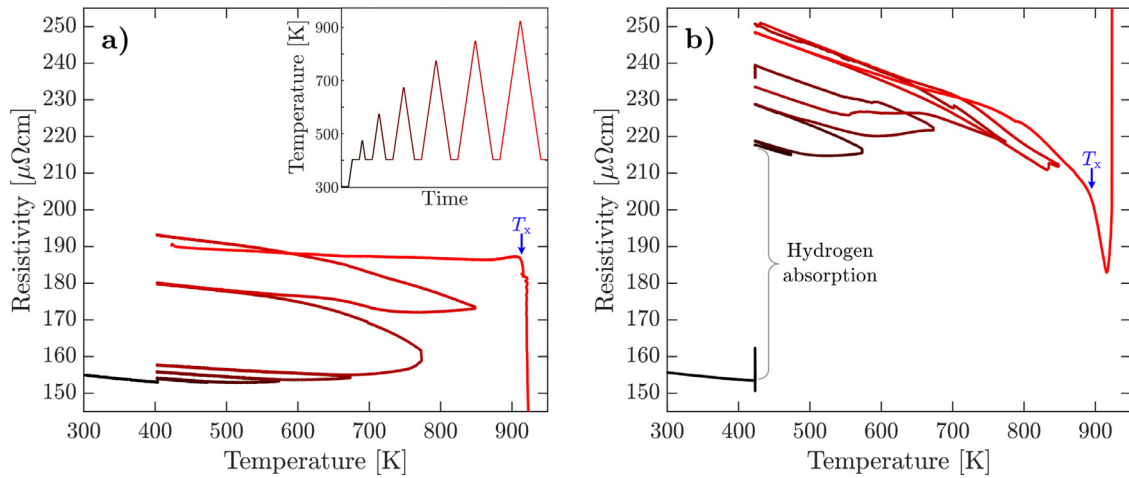


Fig. 3. Resistivity, ρ , as a function of temperature for V₆₇Zr₃₃ (a) and V₄₅Zr₂₂H₃₃ (b), the crystallization temperature is shown by the blue arrow annotated with T_x . The inset shows the temperature profile used for the alloys. (For interpretation of the references to colour in this figure legend, the reader is referred to the web version of this article.)

laxation in the film or migration of oxygen from the cap or substrate to the alloy. The irreversible increase in ρ was observed in all measured samples, both in vacuum and hydrogen atmosphere, and has an increasing trend with increasing Zr content. If oxygen migrated, the intermixing parameter in the reflectivity fits would increase, which is not observed, rendering this possibility less likely. However, the crystallization temperature for V₆₇Zr₃₃ is observed at 913 K in Fig. 3a, where the resistivity abruptly decreases, as expected from the comparably lower resistivity of crystalline materials. The ρ continues to decrease upon cooling (data not shown), which is a signature of a crystalline structure.

For the V₆₇Zr₃₃ alloy in an atmosphere of 95 Torr H₂, shown in Fig. 3b, an initial increase in resistivity can be seen at 423 K due to the absorption of hydrogen. The resistivity increases initially when hydrogen dissolves into metals due to electrons being scattered by the hydrogen and the induced changes in the electronic potential landscape. This has been observed for both crystalline [38] as well as amorphous [39] metals and alloys. The VZr alloy is subsequently annealed, as shown in the inset in Fig. 3a, and the irreversible increase in resistivity above 500 K is again observed. Even though there are differences in the resistivity compared to the V₆₇Zr₃₃ alloy, the V₄₅Zr₂₂H₃₃ alloy remains amorphous until the last annealing cycle, inferred by the measured negative α . The T_x is observed at 894 K, annotated with the blue arrow in the figure, and instead of continuing to decrease, a sharp increase is observed. We attribute the sharp increase after the crystallization event to one or two possible processes. Either the sample oxidized shortly after crystallization, or it cracked due to excessive stresses induced by the presence of hydrogen in or between the crystalline grains. A rapid decay of intensity and the absence of total thickness oscillations past 0.15 Q (2.2 degrees 2 θ) observed in subsequent XRR measurements confirms a high sample roughness. A similar behavior is observed for the V₅₀Zr₅₀ alloy, where ρ rapidly increases after crystallization and a larger sample roughness is deduced from the XRR patterns, whereas no sign of cracking is observed for the V- and Zr-rich alloys. An extended discussion on the XRR data and cracking of the film is provided in the supplementary information.

The T_x for all alloys are shown in Fig. 4a, where it can be seen that the crystallization temperature at first rises with increasing V content and subsequently decreases for V content larger than 50%. The fitted parabola with a center around 58%, indicates that the mid-point compositions are in fact the most thermally stable. The crystallization temperatures for V₃₄Zr₃₃H₃₃, V₄₅Zr₂₂H₃₃, V₅₀Zr₅₀, and V₆₇Zr₃₃ are almost the same. However, the T_x increases up to 150 K for V₅₄Zr₁₃H₃₃ and V₂₂Zr₄₅H₃₃ compared to the alloys without hydrogen, as seen in

Fig. 4a. The additional stability towards the edges of the composition range suggests that it could be possible to synthesize V_xZr_{67-x}H₃₃ alloys with V:Zr ratios that are impossible in the binary alloy. This is because the thermal stability often decreases for alloys with a composition close to the amorphous-to-crystalline boundary [18].

To understand the determined thermal stability, we can consider the physics governing the crystallization process, which is a combined effect of the onset of thermally activated atomic diffusion and the thermodynamic driving force [40]. The difference in Gibbs free energy between the amorphous and crystal phases corresponds to the thermodynamic driving force for crystallization. A smaller difference can relate to an increased stability. The collection of contributions to the free energy for each system, with and without hydrogen, allows us to distinguish the composition and temperature dependency of the driving force. Furthermore, the leading contributors for the thermal stability of the metallic glass can be determined. The thermodynamic driving force for crystallization is shown in Fig. 4b. The energies of V_xZr_{100-x} have the reference states bcc V and hcp Zr and the V_xZr_{67-x}H₃₃ have the reference states bcc V₂H and Zr₂H (lattice gases).

The driving force at 0 K corresponds to the enthalpy of formation of the VZr(H) alloys depicted as black circles/squares in Fig. 4b. A positive enthalpy of formation indicates that the local energy minima of amorphous configurations do not correspond to the most energetically favorable state compared to the corresponding crystalline configuration. However, since the activation energy barrier for crystallization prevents the atoms to reconfigure to the crystalline ground state, long-lived metastable states can exist, and it is therefore necessary to also consider how the free energy changes with temperature to explain the thermal stability of the glass. The enthalpy is considerably lower for the V_xZr_{67-x}H₃₃ alloys compared to the V_xZr_{100-x} alloys, which already suggests a higher stability. As temperature increases, the magnitude of the driving force decreases for all considered systems, and the shape of the driving force for the V_xZr_{67-x}H₃₃ alloys become increasingly convex. The center compositions are hence the most stable, which is observed in the measured crystallization temperatures, see Fig. 4a.

For the V_xZr_{100-x} alloys, the concave curve starts to flatten, but does not change to a convex shape in a temperature range below the determined crystallization temperatures. This demonstrates that the considered contributions to the Gibbs free energy, and particularly the entropy term, are not enough to explain the thermal stability of the V_xZr_{100-x} alloys. We propose that an excess configurational entropy has been neglected, corresponding to the entropy of atomic pair correlations, which can be calculated using the pair distribution functions of alloys [41].

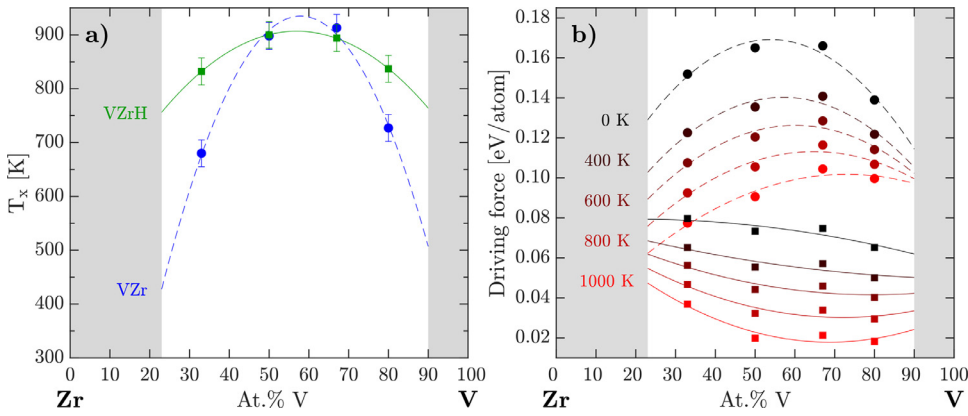


Fig. 4. Crystallization temperatures in vacuum and 95 Torr hydrogen are shown in (a). Solid and dashed lines are parabolic fits and are guides to the eye. The V_xZr_{100-x} and $V_xZr_{67-x}H_{33}$ alloys are depicted as circles and squares in both figures, respectively. The thermodynamic driving forces ($-\Delta G$) determined by first principles are shown in (b) as a function of V/Zr ratio in both systems.

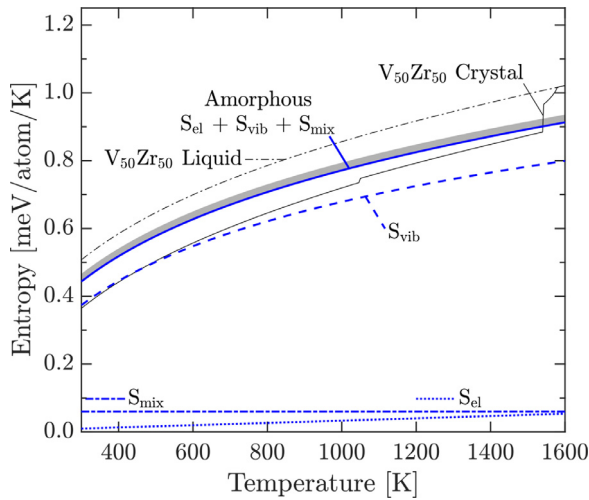


Fig. 5. The calculated partial and total entropy contribution for the $V_{50}Zr_{50}$ composition. The entropy of the corresponding crystal and metastable liquid calculated with Thermo-Calc [43] using the TCHEA3 database are added as illustrative references. The uppermost shaded region correspond to a proposed additional configurational term, that would make the calculated driving force consistent with the measured T_x of the V_xZr_{100-x} alloys.

Furthermore, an excess configurational entropy of a CuZr metallic glass has been measured to be on the order of $0.27 k_B$ (ref. [42]). This supports the idea of an entropy contribution which has not been taken into account for the calculated driving forces herein.

In Fig. 5 we show the total entropy of $V_{50}Zr_{50}$ as a function of temperature. We include the liquid phase and the crystalline phase data from Calphad [43]. The individual contributions to the entropy are shown, including the electronic, phononic and the entropy of mixing. As can be seen in Fig. 5, the entropy of the metallic glass lies in between the liquid and the crystal alloy, as expected. We have indicated in the shaded region, the excess entropy needed to flatten out the stability curve in Fig. 4b at temperatures below the crystallization temperature. This excess entropy is of the same order of magnitude as the configurational entropy found in CuZr near the melting point. This fits the hypothesis that the neglected configurational entropy is indeed the missing contribution that would stabilize the V_xZr_{100-x} glasses.

Furthermore, by adding a third element, hydrogen in this case, increases the entropy of mixing. The total configurational entropy therefore increases, which enhances the thermal stability of the $V_xZr_{67-x}H_{33}$ alloys. However, as described in Section 2, hydrogen-metal correlations are neglected via this approach. The comparable crystallization temperatures for the mid-point compositions between V_xZr_{100-x} and

$V_xZr_{67-x}H_{33}$ can be attributed to a relative decrease of the activation barrier with increasing contents of hydrogen.

The precipitating phases can give additional information as to why alloying with hydrogen has this stabilizing effect. The diffraction patterns for all alloys are shown in Fig. 6a (V_xZr_{100-x}) and 6b ($V_xZr_{67-x}H_{33}$). Solution phases are seen in all crystallized samples with body centred cubic (bcc) for V-rich alloys and hexagonal close packed (hcp) structures for Zr-rich alloys. The bcc and hcp are the two dominant phases for the V-rich ($V_{80}Zr_{20}$) and Zr-rich ($V_{33}Zr_{67}$) alloys respectively, while additional peaks are observed in the remaining two compositions. The position of the (110) and (200) peaks of the bcc V phase match the lattice parameter of pure V of 3.03 \AA , which means that little to no Zr is dissolved in the bcc vanadium lattice. The three peaks at 34, 39, and 56 degrees originate from a face centre cubic (fcc) structured $(V,Zr)O_2$ with a lattice parameter of 4.62 \AA , which has been reported to form in oxygen-depleted environments [44]. The remaining peaks at 30, 50, and 60 deg come from an fcc structure: ZrO_2 , but without V and the lattice parameter is 5.13 \AA , close to the reported [45]. We observe that the peak intensity of the V bcc phase is lower in $V_{33}Zr_{67}$ compared to $V_{50}Zr_{50}$, and likewise the peak intensity of the oxides increase. The Zr-related oxides are not as clearly observed for the samples annealed in the hydrogen atmosphere, while the bcc and hcp are still present, see Fig. 3b. The diffraction patterns from the $V_{80}Zr_{20}H$ and $V_{33}Zr_{67}H$ alloys exhibit similar precipitating phases to those annealed in UHV, with both the bcc V and hcp Zr still being present. In contrast to the UHV annealed samples, the V bcc peak at 42 degrees moves to lower angles with increasing Zr content, which is due to Zr being dissolved into the V bcc lattice in the hydrogen annealed samples, hence the lattice parameter increases around 0.1 \AA from highest to lowest V content. The absence of the oxides can be explained by a lower driving force for oxidation in $V_xZr_{67-x}H_{33}$ alloys compared to V_xZr_{100-x} alloys.

The emerging oxide phases in the UHV annealed samples could suggest that the increased oxidation resistance would also increase the thermal stability. Oxygen is known to reduce thermal stability of metallic glasses [46]. Since the hydrogenated samples do not show any identifiable oxides in the diffraction patterns, one could ascribe the increased stability to the absence of oxygen acting as nucleation sites. This is, however, not the case since the highest T_x is practically the same for the $V_{67}Zr_{33}$ and $V_{50}Zr_{50}$ alloys, where the oxide phases are most predominant, which indicates that the reason cannot be heterogeneous nucleation of crystalline phases. Lastly, there is clear evidence of hydrogen embrittlement in the crystalline $V_xZr_{67-x}H_{33}$ alloys. The XRR data gives clear evidence for cracking of the films, which was only observed for the $V_{34}Zr_{33}H_{33}$ and $V_{45}Zr_{22}H_{33}$ alloys, and not the V_xZr_{100-x} alloys. Furthermore, oxidation was observed in the UHV annealed V_xZr_{100-x} alloys (see Fig. 6a), but not in the $V_xZr_{67-x}H_{33}$ alloys, which is consistent with excluding oxidation as the cause for the resistivity increase. Since the alloy cracks after crystallization in a hydrogen atmosphere and not in

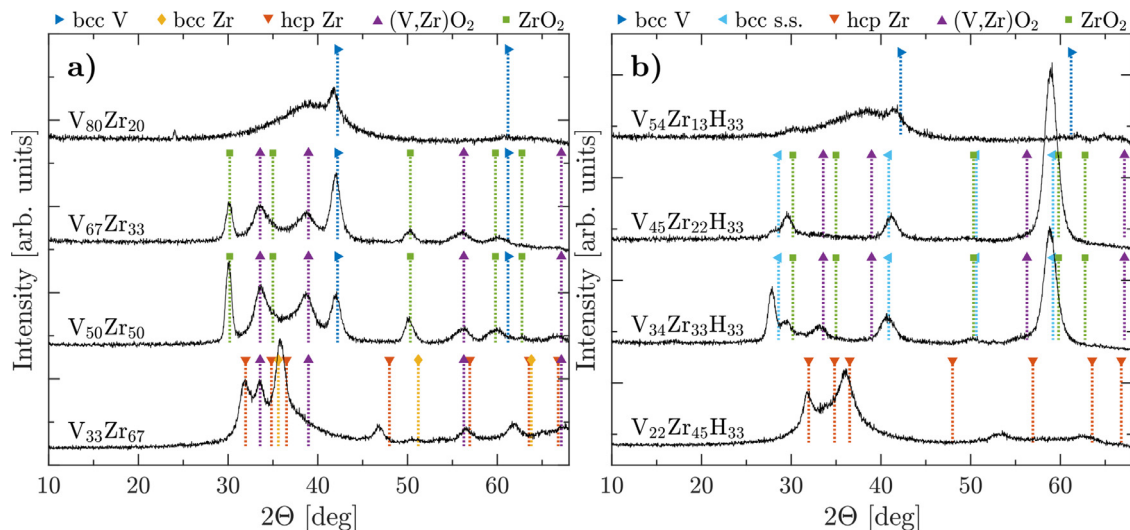


Fig. 6. Diffraction patterns of the crystallized V_xZr_{100-x} alloys (a) and $V_xZr_{67-x}H_{33}$ alloys (b), each value of x keeps the V to Zr ratio constant for the alloys with and without hydrogen. The positions of the diffraction peaks originating from the crystalline phases are shown by the lines and markers.

vacuum, we conclude that the amorphous $V_xZr_{67-x}H_{33}$ alloy can store more hydrogen compared to crystalline $V_xZr_{67-x}H_{33}$ without mechanical failure.

4. Conclusions

The thermal stability is increased and oxygen uptake is reduced by alloying V_xZr_{100-x} with hydrogen. The crystallization temperature increases by up to 150 K in $V_xZr_{67-x}H_{33}$ compared to the V_xZr_{100-x} alloys. Alloys with higher resistivity have higher thermal stability, which opens up the possibility of screening alloys through resistivity measurements to find the highest stability in a system [47].

The thermodynamic driving force for crystallization of the VZr does not appear to be sufficient to stabilize the alloys. We propose that an extended approach, in which the excess configurational entropy, captured by the correlations of the partial pair distribution functions [41], is a necessary step towards the full explanation of the thermal stability of amorphous materials.

With the addition of hydrogen, the entropy of mixing effectively increased. Its influence in combination with a lower enthalpy of formation results in the thermodynamic driving force naturally becoming lower compared to V_xZr_{100-x} , thus indicating that $V_xZr_{67-x}H_{33}$ alloys should be more thermally stable. The findings suggest that the properties of the $V_xZr_{67-x}H_{33}$ alloys can be dynamically changed during operation in technological applications by tuning the hydrogen concentration. The thermal stability can thus be understood by considering only the thermodynamic driving force for crystallization if the reasoning herein is valid. The reasoning can be validated by determining the thermodynamic driving forces of different material systems, which are currently unavailable. Determination of the Gibbs energies, which can be combined with kinetic considerations, are necessary steps toward a complete description of the crystallization process in metallic glasses.

Declaration of Competing Interest

The authors declare that they have no known competing financial interests or personal relationships that could have appeared to influence the work reported in this paper.

Acknowledgments

The authors gratefully acknowledge the Swedish Research council (VR – Vetenskapsrådet) grant number 2018-05200 for funding the work

and the Swedish Energy Agency grant 2020-005212. G.K.P. also acknowledges the Carl-Tryggers foundation grants CTS 17:350 and CTS 19:272 for financial support. The computations were enabled by resources provided by the Swedish National Infrastructure for Computing (SNIC), partially funded by the Swedish Research Council through grant agreement no. 2018-05973.

Supplementary material

Supplementary material associated with this article can be found, in the online version, at doi:10.1016/j.mtl.2022.101496.

References

- [1] L. Tian, Y.-Q. Cheng, Z.-W. Shan, J. Li, C.-C. Wang, X.-D. Han, J. Sun, E. Ma, Approaching the ideal elastic limit of metallic glasses, *Nat. Commun.* 3 (1) (2012) 609, doi:10.1038/ncomms1619.
- [2] Q.K. Jiang, P. Liu, Y. Ma, Q.P. Cao, X.D. Wang, D.X. Zhang, X.D. Han, Z. Zhang, J.Z. Jiang, Super elastic strain limit in metallic glass films, *Sci. Rep.* 2 (1) (2012) 852, doi:10.1038/srep00852.
- [3] W.L. Johnson, Bulk glass-forming metallic alloys: science and technology, *MRS Bull.* 24 (10) (1999) 42–56, doi:10.1557/s0883769400053252.
- [4] G. Libowitz, A. Maeland, Interactions of hydrogen with metallic glass alloys, *J. Less Common Met.* 101 (1984) 131–143, doi:10.1016/0022-5088(84)90091-2.
- [5] M.B. Djukic, G.M. Bakic, V.S. Zeravcic, A. Sedmak, B. Rajcic, The synergistic action and interplay of hydrogen embrittlement mechanisms in steels and iron: localized plasticity and decohesion, *Eng. Frac. Mech.* 216 (2019) 106528, doi:10.1016/j.engfracmech.2019.106528.
- [6] S. Jayalakshmi, S. Park, K. Kim, E. Fleury, D. Kim, Studies on hydrogen embrittlement in Zr- and Ni-based amorphous alloys, *Mater. Sci. Eng. A* 449 (2007) 920–923, doi:10.1016/j.msea.2006.02.417.
- [7] J. Howard, K. Carlson, D. Chidambaram, High-temperature metallic glasses: status, needs, and opportunities, *Phys. Rev. Mater.* 5 (4) (2021) 040301, doi:10.1103/PhysRevMaterials.5.040301.
- [8] S.N. Paglieri, N.K. Pal, M.D. Dolan, S.-M. Kim, W.-M. Chien, J. Lamb, D. Chandra, K.M. Hubbard, D.P. Moore, Hydrogen permeability, thermal stability and hydrogen embrittlement of Ni-Nb-Zr and Ni-Nb-Ta-Zr amorphous alloy membranes, *J. Membr. Sci.* 378 (1–2) (2011) 42–50, doi:10.1016/j.memsci.2011.04.049.
- [9] E.L. Schlapbach, *Topics in Applied Physics: Hydrogen in Intermetallic Compounds II*, vol. 67, Springer-Verlag, 1992.
- [10] N. Ismail, A. Gebert, M. Uhlemann, J. Eckert, L. Schultz, Effect of hydrogen on $Zr_{65}Cu_{17.5}Al_{3}Ni_{10}$ metallic glass, *J. All. Com.* 314 (1–2) (2001) 170–176, doi:10.1016/S0925-8388(00)01211-1.
- [11] J.S. Cantrell, R.C. Bowman, G. Bambakidis, Thermal stability of hydrides of disordered and amorphous alloys, in: *Hydrogen in Disordered and Amorphous Solids*, vol. 136, Springer US, Boston, MA, 1986, pp. 185–202, doi:10.1007/978-1-4899-2025-6_17.
- [12] D. Peng, M. Yan, J. Sun, J. Shen, Y. Chen, D. McCartney, Enhanced thermal stability by pre-charged hydrogen of a Zr-based bulk metallic glass, *J. Alloys Compd.* 400 (1–2) (2005) 197–201, doi:10.1016/j.jallcom.2005.04.005.

- [13] S.-i. Yamaura, A. Inoue, Effect of surface coating element on hydrogen permeability of melt-spun $\text{Ni}_{40}\text{Nb}_{20}\text{Ta}_5\text{Zr}_{30}\text{Co}_{50}$ amorphous alloy, *J. Membr. Sci.* 349 (1–2) (2010) 138–144, doi:[10.1016/j.memsci.2009.11.037](https://doi.org/10.1016/j.memsci.2009.11.037).
- [14] M. Lucaci, D. Patroi, V. Tsakiris, M.V. Lungu, E. Manta, A. Iorga, Studies on Fe-Cr-Ni-Si-B bulk metallic glass for automotive applications, *Adv. Mat. Res.* 1114 (2015) 68–75, doi:[10.4028/www.scientific.net/AMR.1114.68](https://doi.org/10.4028/www.scientific.net/AMR.1114.68).
- [15] R. Gemma, M.t. Baben, A. Pundt, V. Kapaklis, B. Hjörvarsson, The impact of nanoscale compositional variation on the properties of amorphous alloys, *Sci. Rep.* 10 (1) (2020) 11410, doi:[10.1038/s41598-020-67495-4](https://doi.org/10.1038/s41598-020-67495-4).
- [16] C. Cao, D. Ding, D. Zhao, E. Axinte, H. Bai, W. Wang, Correlation between glass transition temperature and melting temperature in metallic glasses, *Mater. Des.* 60 (2014) 576–579, doi:[10.1016/j.matdes.2014.04.021](https://doi.org/10.1016/j.matdes.2014.04.021).
- [17] D. Polk, Structural model for amorphous metallic alloys, *Scr. Metall.* 4 (2) (1970) 117–122, doi:[10.1016/0036-9748\(70\)90175-4](https://doi.org/10.1016/0036-9748(70)90175-4).
- [18] M. Kaplan, G.K. Pálsson, D.M. Holzapfel, J.M. Schneider, B. Hjörvarsson, Phase formation and thermal stability of amorphous ZrNbCrMo thin films, *J. Non-Cryst. Solids* X 9 (2021) 100061, doi:[10.1016/j.nocx.2021.100061](https://doi.org/10.1016/j.nocx.2021.100061).
- [19] A. Inoue, Stabilization of metallic supercooled liquid and bulk amorphous alloys, *Acta Mater.* 48 (1) (2000) 279–306, doi:[10.1016/s1359-6454\(99\)00300-6](https://doi.org/10.1016/s1359-6454(99)00300-6).
- [20] S. Hara, K. Sakaki, N. Itoh, H.-M. Kimura, K. Asami, A. Inoue, An amorphous alloy membrane without noble metals for gaseous hydrogen separation, *J. Membr. Sci.* 164 (1–2) (2000) 289–294, doi:[10.1016/s0376-7388\(99\)00192-1](https://doi.org/10.1016/s0376-7388(99)00192-1).
- [21] S. Eickert, H. Hecht, G.v. Minnigerode, Formation area of amorphous thin V-Zr films prepared by cocondensation on hot substrates, *Z. Phys. B* 88 (1) (1992) 35–38, doi:[10.1007/bf01573835](https://doi.org/10.1007/bf01573835).
- [22] D. King, S. Middleburgh, A. Liu, H. Tahini, G. Lumpkin, M. Cortie, Formation and structure of V-Zr amorphous alloy thin films, *Acta Mater.* 83 (2015) 269–275, doi:[10.1016/j.actamat.2014.10.016](https://doi.org/10.1016/j.actamat.2014.10.016).
- [23] Y. Wang, G.K. Pálsson, H. Raanaei, B. Hjörvarsson, The influence of amorphous Al_2O_3 coating on hydrogen uptake of materials, *J. All. Com.* 464 (1–2) (2008) L13–L16, doi:[10.1016/j.jallcom.2007.10.045](https://doi.org/10.1016/j.jallcom.2007.10.045).
- [24] M. Björck, G. Andersson, GenX: an extensible X-ray reflectivity refinement program utilizing differential evolution, *J. Appl. Crystallogr.* 40 (6) (2007) 1174–1178, doi:[10.1107/s0021889807045086](https://doi.org/10.1107/s0021889807045086).
- [25] F.M. Smits, Measurement of sheet resistivities with the four-point probe, *Bell Syst. Techn. J.* 37 (3) (1958) 711–718, doi:[10.1002/j.1538-7305.1958.tb03883.x](https://doi.org/10.1002/j.1538-7305.1958.tb03883.x).
- [26] E. Holmström, N. Bock, T. Peery, E. Chisolm, R. Lizárraga, G.D. Lorenzi-Venneri, D. Wallace, Structure discovery for metallic glasses using stochastic quenching, *Phys. Rev. B* 82 (2) (2010) 024203, doi:[10.1103/physrevb.82.024203](https://doi.org/10.1103/physrevb.82.024203).
- [27] W. Kohn, L.J. Sham, Self-consistent equations including exchange and correlation effects, *Phys. Rev.* 140 (4A) (1965) A1133–A1138, doi:[10.1103/physrev.140.a1133](https://doi.org/10.1103/physrev.140.a1133).
- [28] P. Hohenberg, W. Kohn, Inhomogeneous electron gas, *Phys. Rev.* 136 (3B) (1964) B864–B871, doi:[10.1103/physrev.136.b864](https://doi.org/10.1103/physrev.136.b864).
- [29] G. Kresse, J. Furthmüller, Efficient iterative schemes for ab initio total-energy calculations using a plane-wave basis set, *Phys. Rev. B* 54 (16) (1996) 11169–11186, doi:[10.1103/physrevb.54.11169](https://doi.org/10.1103/physrevb.54.11169).
- [30] G. Kresse, J. Furthmüller, Efficiency of ab-initio total energy calculations for metals and semiconductors using a plane-wave basis set, *Comput. Mater. Sci.* 6 (1) (1996) 15–50, doi:[10.1016/0927-0256\(96\)00008-0](https://doi.org/10.1016/0927-0256(96)00008-0).
- [31] G. Kresse, J. Hafner, Ab initio molecular dynamics for liquid metals, *Phys. Rev. B* 47 (1) (1993) 558–561, doi:[10.1103/physrevb.47.558](https://doi.org/10.1103/physrevb.47.558).
- [32] J.P. Perdew, K. Burke, M. Ernzerhof, Generalized gradient approximation made simple, *Phys. Rev. Lett.* 77 (18) (1996) 3865–3868, doi:[10.1103/physrevlett.77.3865](https://doi.org/10.1103/physrevlett.77.3865).
- [33] M. Methfessel, A.T. Paxton, High-precision sampling for Brillouin-zone integration in metals, *Phys. Rev. B* 40 (6) (1989) 3616–3621, doi:[10.1103/physrevb.40.3616](https://doi.org/10.1103/physrevb.40.3616).
- [34] A. Togo, I. Tanaka, First principles phonon calculations in materials science, *Scr. Mater.* 108 (2015) 1–5, doi:[10.1016/j.scriptamat.2015.07.021](https://doi.org/10.1016/j.scriptamat.2015.07.021).
- [35] M. Hillert, The compound energy formalism, *J. Alloys Com.* 320 (2) (2001) 161–176, doi:[10.1016/S0925-8388\(00\)01481-X](https://doi.org/10.1016/S0925-8388(00)01481-X).
- [36] J.M. Schneider, How high is the entropy in high entropy ceramics? *J. Appl. Phys.* 130 (15) (2021) 150903, doi:[10.1063/5.0062523](https://doi.org/10.1063/5.0062523).
- [37] J.H. Mooij, Electrical conduction in concentrated disordered transition metal alloys, *Phys. Status Solidi A* 17 (2) (1973) 521–530, doi:[10.1002/pssa.2210170217](https://doi.org/10.1002/pssa.2210170217).
- [38] J. Pryde, I. Tsong, A theory of the resistivity of high-concentration interstitial alloys with application to the tantalum-hydrogen and tantalum-deuterium systems, *Acta Metall.* 19 (12) (1971) 1333–1338, doi:[10.1016/0001-6160\(71\)90070-8](https://doi.org/10.1016/0001-6160(71)90070-8).
- [39] Y. Yamada, K. Tanaka, Electrical resistivity change during hydrogen charging and subsequent heating in Zr-Ni alloy glasses, *Trans. Jpn. Inst. Metals* 27 (6) (1986) 409–415, doi:[10.2320/matertrans1960.27.409](https://doi.org/10.2320/matertrans1960.27.409).
- [40] C.A. Angell, Formation of glasses from liquids and biopolymers, *Science* 267 (5206) (1995) 1924–1935, doi:[10.1126/science.267.5206.1924](https://doi.org/10.1126/science.267.5206.1924).
- [41] M.C. Gao, M. Widom, Information entropy of liquid metals, *J. Phys. Chem. B* 122 (13) (2018) 3550–3555, doi:[10.1021/acs.jpcc.7b10723](https://doi.org/10.1021/acs.jpcc.7b10723).
- [42] H.L. Smith, C.W. Li, A. Hoff, G.R. Garrett, D.S. Kim, F.C. Yang, M.S. Lucas, T. Swanwood, J.Y.Y. Lin, M.B. Stone, D.L. Abernathy, M.D. Demetriou, B. Fultz, Separating the configurational and vibrational entropy contributions in metallic glasses, *Nat. Phys.* 13 (9) (2017) 900–905, doi:[10.1038/nphys4142](https://doi.org/10.1038/nphys4142).
- [43] J.-O. Andersson, T. Helander, L. Höglund, P. Shi, B. Sundman, Thermo-Calc & DICTRA, computational tools for materials science, *Calphad* 26 (2) (2002) 273–312, doi:[10.1016/S0364-5916\(02\)00037-8](https://doi.org/10.1016/S0364-5916(02)00037-8).
- [44] P. Keuter, A.L. Ravensburg, M. Hans, S. Karimi Aghda, D.M. Holzapfel, D. Primetzhofer, J.M. Schneider, A proposal for a composite with temperature-independent thermophysical properties: $\text{HfV}_2\text{-HfV}_2\text{O}_7$, *Materials* 13 (21) (2020) 5021, doi:[10.3390/ma13215021](https://doi.org/10.3390/ma13215021).
- [45] D. Wang, Y. Guo, K. Liang, K. Tao, Crystal structure of zirconia by Rietveld refinement, *Sci. China Ser. A Math.* 42 (1) (1999) 80–86, doi:[10.1007/BF02872053](https://doi.org/10.1007/BF02872053).
- [46] J. Eckert, N. Mattern, M. Zinkevitch, M. Seidel, Crystallization behavior and phase formation in Zr-Al-Cu-Ni metallic glass containing oxygen, *Mater. Trans. JIM* 39 (6) (1998) 623–632, doi:[10.2320/matertrans1989.39.623](https://doi.org/10.2320/matertrans1989.39.623).
- [47] M.-X. Li, S.-F. Zhao, Z. Lu, A. Hirata, P. Wen, H.-Y. Bai, M. Chen, J. Schroers, Y. Liu, W.-H. Wang, High-temperature bulk metallic glasses developed by combinatorial methods, *Nature* 569 (7754) (2019) 99–103, doi:[10.1038/s41586-019-1145-z](https://doi.org/10.1038/s41586-019-1145-z).